Contents lists available at ScienceDirect

Applied Catalysis B: Environmental

CrossMark

Enhancement of visible photocatalytic activity via Ag@C$_3$N$_4$ core–shell plasmonic composite

Xiaojuan Bai, Ruilong Zong, Cuixia Li, Di Liu, Yanfang Liu, Yongfa Zhu[*]

Department of Chemistry, Beijing Key Laboratory for Analytical Methods and Instrumentation, Tsinghua University, Beijing 100084, China

ARTICLE INFO

ABSTRACT

A novel and simple synthetic approach toward core–shell Ag@C$_3$N$_4$ nanocomposites is developed. Ag@C$_3$N$_4$ core–shell nanostructures were formed via reflux treatment of Ag nanoparticles with graphitic C$_3$N$_4$ nanosheets in methanol. The core–shell hybrid photocatalysts showed dramatic photoinduced electron–hole separation efficiency and photocatalytic activity under visible light irradiation. The photocurrent intensity, photocatalytic activity for the photodegradation of methylene blue (MB) and hydrogen evolution reaction of Ag@C$_3$N$_4$ were about 4, 1.8 and 30 times as that of pure C$_3$N$_4$ sample, respectively. The enhanced photocatalytic activity for core–shell Ag@C$_3$N$_4$ originated from a combined result of the localized surface plasmon resonance (LSPR) effect for Ag and hybrid effect from C$_3$N$_4$, resulting in the coupling interaction of the enhanced light absorption intensity, high separation efficiency of photogenerated electrons–holes, longer lifetime of charge carriers and its favorable adsorptivity.

1. Introduction

Photoinduced charge separation in semiconductor nanoparticles and nanostructured films provides the basis for photocatalytic degradation of organic contaminants [1], the dye-sensitized photochemical solar cells [2], and chemical sensors [3]. Charge recombination within the particle or at the grain boundary often limits the efficiency of light energy conversion. By employing two different semiconductors [4] or semiconductor–metal composites [5], one can suppress the charge recombination process to some extent. Previous studies have shown that, when a gold nanoparticle comes in contact with a photoexcited semiconductor, the two particles undergo charge equilibration [6]. The shift in the Fermi level toward the conduction band energy enhances the catalytic efficiency of the composite system [7].

Noble metal nanoparticles are known to exhibit various colors arising from surface plasmon absorption [8] and size-dependent specific catalytic [9] and optical [10] properties. Although the nanoparticles have attracted attention in diverse fields of science and technology [11] because of their interesting properties, they are hardly usable by themselves since they are poor at dispersion stability and tend to aggregate in the medium. In most of the catalytic studies metal nanoparticles are dispersed on an oxide surface [12–14]. Such a catalyst structure, though effective, result in exposing both metal to reactants and the surrounding medium. Corrosion

or dissolution of the noble metal particles during the operation of a photocatalytic reaction is likely to limit the use of noble metal Ag [15]. In addition, the metal NPs are only in point contact with the semiconductor matrix. Moreover, the observed enhancement of photocatalytic activity arises from a combination of effects due to the localized surface plasmon resonance (LSPR) and self-catalysis of the metal [16]. A better synthetic design can significantly improve the catalytic performance of semiconductor–metal composite. The metal-core@semiconductor-shell NPs are developed as plasmonic photocatalysts and they contain several advantages. First, such core–shell architecture effectively protects the metal NPs from corrosion. Second, it maximizes the metal–support interaction through the three-dimensional contact between the metal core and the semiconductor shell, thereby facilitating the plasmonic energy transfer processes. Last, the local electromagnetic field of the LSPR penetrates the shell, which can be used to tune the center wavelength of the LSPR [17]. Silica has been widely employed as a shell to protect Ag nanoparticles and stabilize them against chemical corrosion. Preparation and characterization of Ag@SiO$_2$ core–shell cluster have been reported for metal core-oxide shell clusters [18]. Kamat et al. investigated the charge separation, charge storage, and interfacial charge-transfer steps that follow excitation of the TiO$_2$ shell in Ag@TiO$_2$ composites. They demonstrated the photoinduced charging and dark discharging of electrons in a silver core-semiconductor shell structure. The shift in surface plasmon band serves as a measure to determine the number of electrons stored in the metal core [19]. Sakai et al. also reported a new method aims to prepare highly dispersible core/shell-type Ag@TiO$_2$ [20]. Li et al. developed an efficient visible-light

* Corresponding author. Tel.: +86 10 62787601; fax: +86 10 62787601.
E-mail address: zhuyf@tsinghua.edu.cn (Y. Zhu).

plasmonic photocatalyst Ag@Cu_2O core–shell heterostructure, which allows for tunable light absorption over the entire visible-light region by tailoring the shell thickness [16]. Recently, Dong et al. prepared Ag@AgCl plasmonic photocatalyst by a facile green route and demonstrated that •O_2^- and Cl^0 are responsible for the rapid degradation of organic pollutants under visible-light irradiation [21].

Although significant advances have been made in recent years to design Ag core-semiconductor shell clusters and concern loaded-type Ag-C_3N_4 composite particles [22,23], no report has so far dealt with the preparation of individual core/shell-type M@C_3N_4 nanocapsules. Carbon nitride, which is essentially composed of covalent bondings, has received a large interest as the most promising candidate to complement carbon in photocatalytic applications and possesses a very high thermal and chemical stability and has attracted extensive attentions due to its outstanding mechanical, electrical, thermal, and optical properties [24–27]. There have several reports demonstrated the photocatalytic performance for H_2 and O_2 evolution over C_3N_4 photocatalyst via water splitting [28–31]. Ge et al. demonstrated that Ag/C_3N_4 exhibited enhanced photocatalytic activity in degradation of methyl orange and hydrogen evolution [22]. However, the photocatalytic activity of the loaded-type Ag-C_3N_4 is still needed to be improved due to the fast recombination of photogenerated charge carriers. Furthermore, as previously mentioned, corrosion or dissolution of the noble metal Ag particles during the operation of a photocatalytic reaction is likely to limit the use of noble metal Ag. Therefore, the present study aims to prepare highly dispersible core/shell-type Ag@C_3N_4 nanostructures and study the mechanism of enhanced photocurrent intensity as well as photocatalytic efficiency, emphatically.

In this work, a novel and simple synthetic approach toward core–shell Ag@C_3N_4 nanocomposites is presented. The effect of Ag amount coated by C_3N_4 on photocatalytic activity and optical properties were investigated in detail. The core–shell photocatalyst Ag@C_3N_4 was demonstrated to be photostable after cycle photocatalytic experiment. The photocurrent intensity, photocatalytic activity for the photodegradation of methylene blue and hydrogen evolution reaction of Ag@C_3N_4 under visible light were about 4, 1.8 and 30 times as that of pure C_3N_4 sample, respectively. To the best of our knowledge, this is the first report on visible light photoactivity enhancement of Ag@C_3N_4 core–shell structures. The hybrid and plasma effects between Ag and C_3N_4 and the possible mechanisms of enhancement of photocurrent intensity as well as photocatalytic activity were systematically investigated. A better understanding of the charge transfer properties in Ag@C_3N_4 samples is likely to pave the way to develop improved plasmonic photocatalysts for light energy conversion.

2. Experimental

2.1. Materials

The bulk C_3N_4 photocatalysts were synthesized as described in a previous paper [32]. All chemicals were reagent grade and used without further purification. Dicyandiamide (3 g) (Aldrich, 99%) in an open crucible was heated in static air with a ramping rate of 2.3 °C/min to 550 °C where it was held for 4 h. The product was collected and ground into powder in an agate mortar for further characterization and performance measurements. It should be claimed that the widely used "C_3N_4" in the literature is actually nonstoichiometric. Here we use "C_3N_4" to describe the products just to keep consistent with the general usage.

2.2. Synthesis of Ag nanoparticles and C_3N_4 nanosheets

A certain amount of $AgNO_3$ crystal was dissolved in the absolute methanol, the solution was stirred to keep it completely dissolved prior to irradiation with 11 W UV lamp ($\lambda = 254$ nm). After irradiation for 24 h, the solution was dispersed by ultrasonication to prevent Ag nanoparticles aggregated. The ultrathin C_3N_4 nanosheets were obtained by modified liquid exfoliating of as-prepared bulk C_3N_4 in methanol according to the literature [33]. In detail, 100 mg of bulk C_3N_4 powder dispersed in 150 mL methanol, and then ultrasound for about 24 h. The initial formed suspension was then centrifuged at low speed to remove the residual unexfoliated C_3N_4 nanoparticles and large-area nanosheets before used for further study. The stirred rate, ultrasonic time and volume ratio of methanol are important factors in the preparation of the Ag@C_3N_4 clusters.

2.3. Synthesis of Ag@C_3N_4 samples

Core–shell Ag@C_3N_4 photocatalysts were prepared as follows: The obtained Ag nanoparticles solution was added into the C_3N_4 nanosheets suspension. Then Ag nanoparticles and C_3N_4 nanosheets mixture were dispersed by ultrasonication for 30 min and stirred for 2 h at room temperature, and then refluxed with continued stirring. With continued heating of the solution, the color slowly changed from colorless to greenyellow and then to light brown. After 3 h, the color of the suspension turned to dark brown. At this point, the heating was stopped and the suspension was stirred until it cooled to room temperature. With different Ag amount coated by C_3N_4, the color of the suspension and products is different. Ag@C_3N_4 photocatalysts with different Ag raw ratio from 0.3 wt.% to 10.0 wt.% were prepared according to above method. The Ag@C_3N_4 core–shell hybrid photocatalysts were marked as ACN-X, X label as Ag@C_3N_4 mass ratio 0.3, 0.5, 1.0, 2.0, 3.0, 4.0, 6.0, and 10.0.

C_3N_4 and Ag@C_3N_4 electrodes were prepared as follows: 4 mg of as-prepared photocatalyst was suspended in 2 mL ethanol to produce slurry, which was then dip-coated onto a 2 cm × 4 cm indium-tin oxide (ITO) glass electrode. Electrodes were exposed to UV light for 10 h to eliminate ethanol and subsequently calcined at 200 °C for 8 h under N_2 flow (rate = 60 mL/min). All investigated electrodes were of similar thickness (0.8–1.0 μm).

2.4. Characterizations

High resolution transmission electron microscopy (HRTEM) images were obtained by JEOL JEM-2011F field emission transmission electron microscope with an accelerating voltage of 200 kV. To avoid electron beam-induced damage, low-intensity beam was used for collecting selected area electron diffraction (SAED) patterns. X-ray diffraction (XRD) patterns of the powders were recorded at room temperature by a Bruker D8 Advance X-ray diffractometer. The diffuse reflectance absorption spectra (DRS) of the samples were recorded in the range from 250 to 800 nm using a Hitachi U-3010 spectroscope equipped with an integrated sphere attachment and $BaSO_4$ was used as a reference. Raman spectra were recorded on a microscopic confocal Raman spectrometer (Renishaw 1000 NR) with an excitation of 514.5 nm laser light. The room-temperature photoluminescence (PL) spectra of C_3N_4 and Ag@C_3N_4 samples were investigated utilizing the Perkin-Elmer LS55 spectrophotometer equipped with xenon (Xe) lamp with an excitation wavelength of 345 nm. Fourier transform infrared (FTIR) spectra were carried out using Perkin-Elmer spectrometer in the frequency range of 4000–450 cm^{-1} with a resolution of 4 cm^{-1}. X-ray photoelectron spectroscopy (XPS) was measured in a PHI 5300 ESCA system. The beam voltage was 3.0 kV, and the

energy of Ar ion beam was 1.0 keV. The binding energies were normalized to the signal for adventitious carbon at 284.8 eV. The Brunauer–Emmett–Teller (BET) surface area measurements were performed by a micromeritics (ASAP 2010 V5.02H) surface area analyzer. The nitrogen adsorption and desorption isotherms were measured at 77 K after degassing the samples on a Sorptomatic 1900 Carlo Erba Instrument. The electron spin resonance (ESR) signals of radicals spin-trapped by spin-trap reagent 5,5′-dimethyl-1-pirroline-N-oxide (DMPO) (purchased from Sigma Chemical Co.) were examined on a Bruker model ESR JES-FA200 spectrometer equipped with a quanta-Ray Nd:YAG laser system as the irradiation source ($\lambda = 365/420$ nm). To minimize experimental errors, the same type of quartz capillary tube was used for all ESR measurements. The ESR spectrometer was coupled to a computer for data acquisition and instrument control. Magnetic parameters of the radicals detected were obtained from direct measurements of magnetic field and microwave frequency. Zeta-potential measurements were performed using a HORIBA SZ-100 series analyzer. Electrochemical and photoelectrochemical measurements were performed in a three electrode quartz cells with 0.1 M Na_2SO_4 electrolyte solution. Platinum wire was used as counter and saturated calomel electrode (SCE) used as reference electrodes, respectively. And C_3N_4 and Ag@C_3N_4 film electrodes on ITO served as the working electrode. The photoelectrochemical experiment results were recorded with an electrochemical system (CHI-660B, China). The visible irradiation was obtained from a 500 W Xe lamp (Institute for Electric Light Sources, Beijing) with a 420 nm cut-off filter. Potentials are given with reference to the SCE. The photoresponses of the photocatalysts as UV light on and off were measured at 0.0 V. Electrochemical impedance spectra (EIS) were measured at 0.0 V. A sinusoidal ac perturbation of 5 mV was applied to the electrode over the frequency range of 0.05–105 Hz.

3. Photocatalytic experiments

3.1. Photocatalytic activity for degradation of pollutants

The photocatalytic activities were evaluated by the decomposition of methylene blue (MB) under visible light irradiation ($\lambda > 420$ nm). Visible irradiation was obtained from a 500 W Xe lamp (Institute for Electric Light Sources, Beijing) with a 420 nm cutoff filter, and the average visible light intensity was 38 mW/cm^2. 25 mg of photocatalyst was totally dispersed in an aqueous solution of MB (50 mL, 0.01 mM) or phenol (50 mL, 10 ppm). Before irradiation, the suspensions were magnetically stirred in dark for 60 min to get absorption–desorption equilibrium between the photocatalyst and MB (phenol). At certain time intervals, 3 mL aliquots were sampled and centrifuged to remove the particles. The concentration of MB was analyzed by recording the absorbance at the characteristic band of 663 nm using a Hitachi U-3010 UV–vis spectrophotometer and phenol was detected using a HPLC method. To investigate the active species generated in the photocatalytic degradation process, the experiments of free radicals (hydroxyl radical ($\bullet$OH) and hole (h$^+$)) capture were carried out by tert-butylalcohol (tBuOH) and ethylenediamine tetraacetic acid disodium salt (EDTA-2Na), respectively.

3.2. Photocatalytic activity for hydrogen evolution reaction

The photocatalytic gas evolution was conducted in an outer irradiation Pyrex cell with a top window, which was connected to a closed gas-circulating system (equipped with a vacuum line, a gas sampling port that is directly connected to a gas chromatograph). The temperature was maintained at room temperature by providing a flow of cooling water during the photocatalytic

reaction. The 0.1 g of catalyst powder was dispersed by stirring for 1 h in an aqueous solution (200 ml) containing triethanolamine (20 vol.%) as sacrificial electron donor. Before reaction, the system was vacuumed and 2.7 kPa of argon gas was introduced. The reaction was carried out by irradiating the mixture using a 300 W Xe lamp (PLS-SXE300) equipped with an optical filter ($\lambda > 420$ nm) to cut off the light in the ultraviolet region. The evolved amounts of hydrogen were analyzed by a gas chromatograph (TCD, molecular sieve 5A column, argon carrier).

4. Results and discussion

4.1. Core–shell hybrid structure and optical properties

Fig. 1a and b shows the typical TEM images of Ag@C_3N_4 composite particles with 0.5 wt.% and 10 wt.% Ag contents. In these composite particles, 5–15 nm Ag particle (core) is encapsulated within C_3N_4 film (shell) of 60–80 nm thick, the TEM images show a majority of dark images of Ag core in this size regime. It is apparent that each core–shell nanoparticle only contained one Ag core, and almost no particles with multiple Ag cores or without a Ag core were found in this sample. The as-obtained core–shell Ag@C_3N_4 nanoparticles exhibited uniform spherical overall morphology, well-preserving the quasi-spherical shape of the Ag cores (Fig. S1). In order to obtain more detailed growth information of shell formation of the core–shell Ag@C_3N_4 nanoparticles, HRTEM results are shown in Figs. 1c, d and S2a. They show the local crystalline lattices at the heterointerface of the Ag and C_3N_4 shell as indicated by the yellow circle. It is revealed that well-defined interface and continuity between metallic Ag nanoparticles and C_3N_4 shells is indicative of strong interaction between exposed Ag atoms and —C—N—, —C=N— bonds in C_3N_4 shells [34,35]. The spacing between adjacent lattice fringes is 0.24 nm for the Ag core and 0.32 nm for C_3N_4 (shell), which is close to the d spacing of the (1 1 1) plane of metallic Ag ($d = 0.235$ nm; JCPDS No. 089-3722) and C_3N_4 ($d = 0.336$ nm; JCPDS No. 087-1526), revealing that the epitaxial formation of (0 0 2) crystal planes of C_3N_4 near the Ag@C_3N_4 interface due to matching with exposed Ag (1 1 1) planes keeps interfacial energy low [36–38]. We have further performed line-scanned element analysis on individual core–shell Ag@C_3N_4 nanoparticles using EDX spectroscopy. Fig. S2b shows an integrated EDX spectrum along an individual core–shell particle, which clearly shows the presence of Ag, Cu, C and N. On the basis of the above evidence, a possible growth mechanism of the Ag@C_3N_4 core–shell structure is proposed as follows (as shown in Scheme 1): Firstly, Ag nanoparticles are dispersed into the C_3N_4 nanosheets methanol solution. Some C_3N_4 nanosheets are then partially deposited on the surface of Ag nanoparticles to form nucleation sites for subsequent growth of C_3N_4 nanosheets under effects of coordination between Ag which provides unoccupied orbital and N which offers lone pair electron. Secondly, during early stages of the reaction, C_3N_4 nanosheets are formed on the Ag surface under the nucleation effect of Ag nanoparticle. With increasing reaction time, initial spheroidal structure continuously aggregate and crystallize, leading to increasing diameters of the C_3N_4 shell. The process may be attributed to a synergistic interaction of coordination and coupling processes, and then monolayer-coated core coalescence and shell re-encapsulation. Finally, an ideal and uniform core–shell Ag@C_3N_4 nanostructure is formed.

XRD pattern is used to investigate the phase structures of the samples, and the typical diffraction patterns are shown in Fig. 2. The peaks at 13.1° and 27.4° in the XRD patterns of the samples could be indexed to the hexagonal phase of C_3N_4 (JCPDS 087-1526). The peak at 27.4° is due to the stacking of the conjugated aromatic system, which is indexed for graphitic materials as the
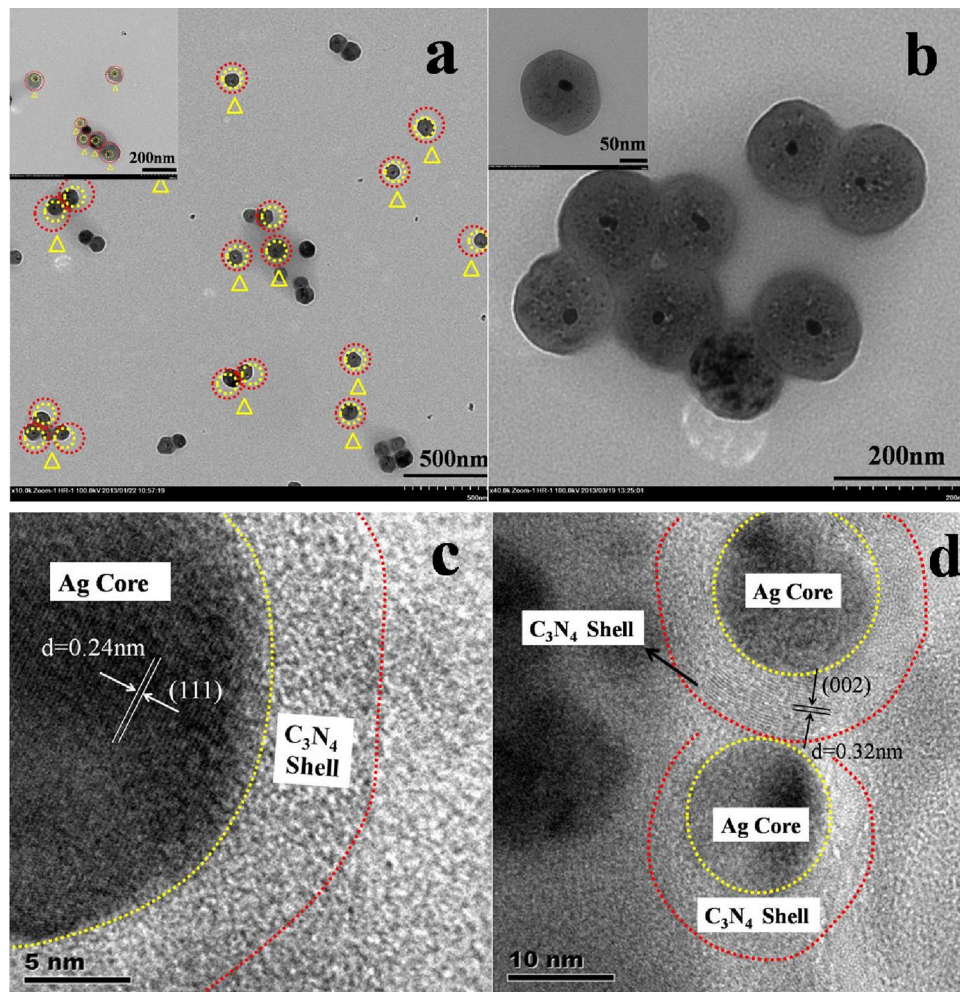
Fig. 1. TEM images of Ag@C_3N_4-0.5 wt.% (a) and Ag@C_3N_4-10 wt.% (b); HRTEM images (c and d) of Ag@C3N4-0.5 wt.% photocatalyst.

(0 0 2) peak of the C_3N_4 [22]. No significant diffraction peaks of any other phases or impurities can be detected in the composite samples, which indicate the introducing of Ag species does not affect the crystal structure of C_3N_4 photocatalysts. However, the diffraction intensities of the peak at 27.4° and 13.1° become weaker with increasing Ag contents, which suggest the diffracted intensity

of C_3N_4 nanosheets becomes weak after exfoliating of bulk C_3N_4 nanoplates. Furthermore, Ag@C_3N_4 samples were found to exhibit the diffraction peaks characteristic of Ag crystal at 38.0° and 44.2°, which is coincided with those for Ag. The peak intensity of Ag for Ag@C_3N_4 samples becomes stronger as the Ag contents increased, which may be explained by Ag plasmonic effects and high uniform dispersion in Ag@C_3N_4 samples [20].

Fig. 3 shows the Raman spectra of C_3N_4 and Ag@C_3N_4 samples. Raman spectroscopy is widely used to study the vibrational properties of carbon related materials. In the Raman spectra within the range 1000–2000 cm^{-1} for C_3N_4 and Ag@C_3N_4 samples, there are two peaks observed at 1347 cm^{-1} (D band) and 1569 cm^{-1} (G band) [39]. The G band corresponds to the symmetric E_{2g} vibrational mode in graphite-like structures and is attributed to graphite-like sp^2 microdomains in the products, while the D band corresponds to disordered sp^2 microdomains introduced by the linking with N atoms [40]. Compared with that of pure C_3N_4, the increased intensity of G band and decreased signal of D band for Ag@C_3N_4 samples indicates the vibrational intensity of ordered graphitic structure is stronger and structural defect becomes weaken. In addition, the peaks located at 974 cm^{-1} and 475 cm^{-1} become stronger than that of pure C_3N_4. In general, Raman intensity can be greatly enhanced by the electromagnetic interaction or coupling between Ag metal nanostructures with proper shape and size. Ling et al. reported that graphite-like materials also have the potential enhancing the Raman effects and found that the Raman enhancement factors can be distinguished through three classes that correspond to
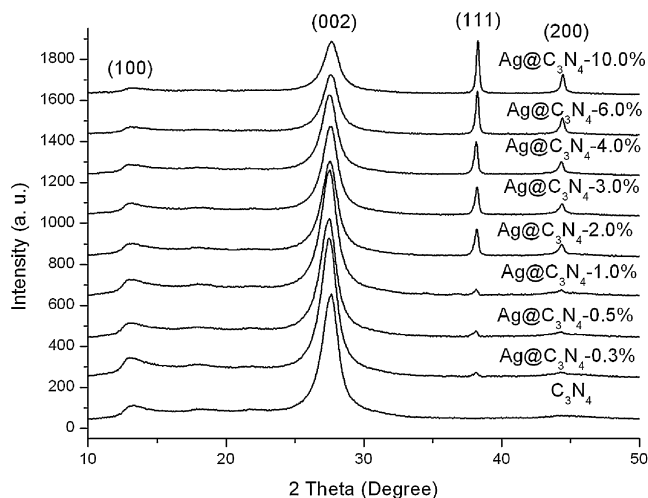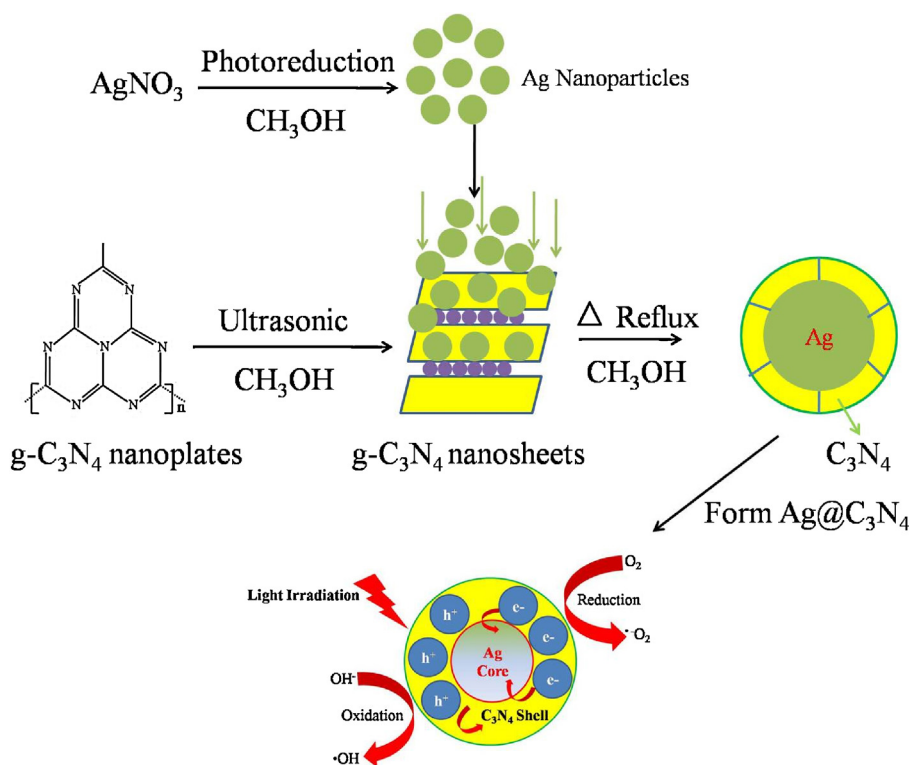

Fig. 2. XRD patterns of the C_3N_4 and Ag@C_3N_4 photocatalysts.

Scheme 1. Schematic drawing illustrating synthetic route and the mechanism of charge separation and photocatalytic process over C_3N_4 and $Ag@C_3N_4$ photocatalysts under light irradiation.

the symmetry of vibrations of the molecule [41]. Therefore, the enhancement of Raman intensity could be attributed to the charge transfer between Ag and the C_3N_4 molecules, originating from the plasma and Raman enhancement effects of Ag nanoparticles and C_3N_4 molecules, respectively. The FTIR result is consistent with the Raman spectra (Fig. S3).

The absorption range of light plays an important role in the photocatalysis, especially for the visible light photodegradation of contaminants. As shown in Fig. 4a, which shows the UV–vis diffuse reflectance spectroscopy (DRS) of pure C_3N_4 and core–shell $Ag@C_3N_4$, there is about red shift of ca.15–39 nm in the absorption edge and enhanced absorption intensity of $Ag@C_3N_4$ samples, which could be responsible for the visible-light induced photocatalytic activity. While the powder colors shift from yellowish to
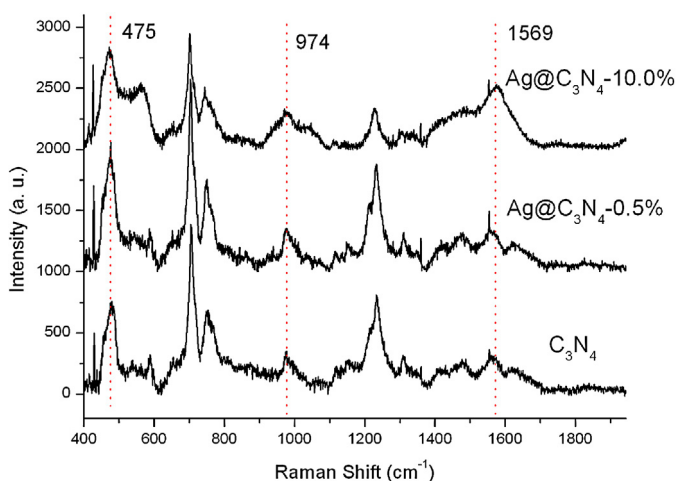

Fig. 3. Raman spectra of the C_3N_4 and $Ag@C_3N_4$ photocatalysts.

dark brown with increasing Ag loading. This phenomenon could be attributed to a charge-transfer transition between the Ag species and the C_3N_4 sample [22]. As shown in Fig. 4b, the absorption red-shift may be attributed to bigger sizes of core–shell $Ag@C_3N_4$ nanoparticles due to the coating growth along the edge of C_3N_4 shell. Compared with pure C_3N_4, core–shell $Ag@C_3N_4$ nanoparticles have a weak and broad plasmon absorption peaks at 407 and 600 nm, meanwhile, the peak at 334 nm of pure C_3N_4 becomes weak, which may be attributed to the localized surface plasmon resonance (LSPR) response of Ag cores, and a significant red-shift against pure C_3N_4, probably due to a strong interfacial electronic coupling between C_3N_4 shells and Ag nanoparticles, reflecting Ag nanoparticles surrounded by high-refractive-index C_3N_4 shells [20,42,43]. The weak LSPR response is attributed to the thick C_3N_4 shells for individual core–shell $Ag@C_3N_4$ nanoparticles [44]. In addition, the LSPR position and the plasmonic field intensity are highly sensitive to both the shape and the size of the cores, as well as the dielectric constant of the surrounding medium. The plasmon dampening rate is reduced, leading to differences in the oscillator strength [45]. Therefore, the intensity of absorption peaks at 407 and 600 nm for $Ag@C_3N_4$ becomes more stronger as the Ag contents increased.

The interaction between individual nanoparticles in the metal-semiconductor core–shell nanostructures may be monitored by determining the changes in the emission properties of the fluorescent component as a consequence of the assemblage process. Enhancement of emission may occur as a result of amplification of the electric field by plasmon resonance, where as emission quenching may be indicative of energy or charge transfer from the semiconductor to metal nanoparticles [46]. Fig. 5 shows the PL spectra of the C_3N_4 and the $Ag@C_3N_4$ excited at 430 nm are presented. The emission peak of $Ag@C_3N_4$ samples at around 459 nm was slightly broadened and quenched in intensity as Ag contents increased, indicating efficient interfacial electron transfer from the
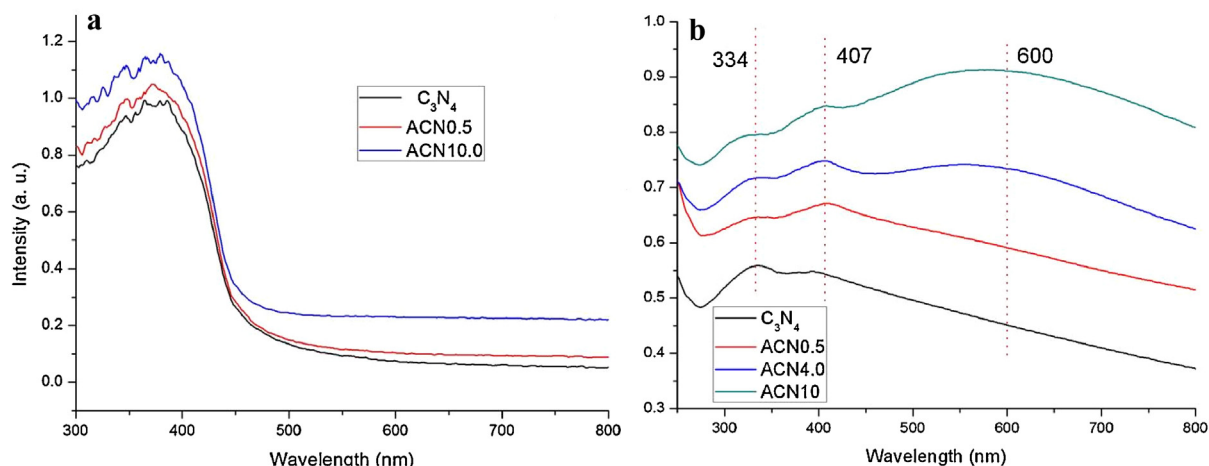
Fig. 4. Diffuse reflectance absorption spectra and UV–vis optical properties of the C_3N_4 and $Ag@C_3N_4$ photocatalysts.

conduction band of C_3N_4 to the Ag species, which act as electron sinks and hamper the recombination of photoinduced carriers [47]. The result corresponds to an efficient charge separation in the $Ag@C_3N_4$, which would have an effect on the photoelectric and photocatalytic properties of the material.

4.2. Photocatalytic activity and photocurrent response

Fig. 6a shows the photocatalytic activity of C_3N_4 and $Ag@C_3N_4$ samples for photodegradation of MB under visible light irradiation, respectively. Significant differences in the catalytic behaviors were observed, and the photodegradation process was fit to pseudo-first-order kinetics in which the value of rate constant k is equal to the corresponding slope of the fitting line. The blank test confirms that MB is only slightly degraded in the absence of catalysis or in the dark, indicating that the photolysis and adsorption effects can be ignored (Fig. S4). Under visible light irradiation (Fig. 6a), the $Ag@C_3N_4$ sample with 0.5 wt.% Ag had the highest activity, which was about 1.8 times as that of pure C_3N_4 sample. Photocatalytic results demonstrated that the loading amount of Ag had a great influence on the photocatalytic activity of the as-prepared samples. When the Ag content was relatively low (<0.5 wt.%), the photocatalytic activity of $Ag@C_3N_4$ increased continuously. Alternatively, when the Ag content is relatively high (>1.0 wt.%), the photocatalytic activity of $Ag@C_3N_4$ decreased with increasing Ag content. This can be explained from that the excess Ag species may act as a recombination center, or cover the active sites of

C_3N_4 shell and reduce the availability of pollutant adsorption, then reduce the efficiency of charge separation [22]. Therefore, it is important to make a balance between the active trapping sites favoring the inhibition of the recombination of electron–hole pairs and fewer trapped parts leading to a lower capacity for the separation of interfacial charge thansfer. According to the results, the photocatalytic activity of $Ag@C_3N_4$ is effectively enhanced compared with that of pure C_3N_4, the reason should be attributed to the chemical interaction between C_3N_4 and Ag, which takes an important role in the enhancement of photocatalytic performance. As shown in Fig. 6b, it can be observed that the core–shell $Ag@C_3N_4$ samples exhibit enhanced photocatalytic performance of photodegration of methyl orange (MO) and phenol, which is about 2.1 and 2.2 times as that of pure C_3N_4 sample. Based on these results, it can be concluded that the incorporation of Ag metal into the photoactive shell of C_3N_4 could significantly enhance the photocatalytic activity of the semiconductor C_3N_4 toward various probe molecules in environment purifying under visible light illumination. The result of photostability experiment shows that the photocatalytic activity of $Ag@C_3N_4$-0.5% exhibits only 4.6% decrease after running for four cycles (about 48 h irradiation), indicating that $Ag@C_3N_4$-0.5% is a stable visible light photocatalyst (Fig. S5).

Fig. 7a shows the results of the transient photocurrent response obtained from pure C_3N_4 and $Ag@C_3N_4$ samples. The photocurrent intensity remains at a constant value when the light is on and rapidly decreases to zero as long as the light is turned off. It is obvious to observe that the photocurrent over $Ag@C_3N_4$ is greatly
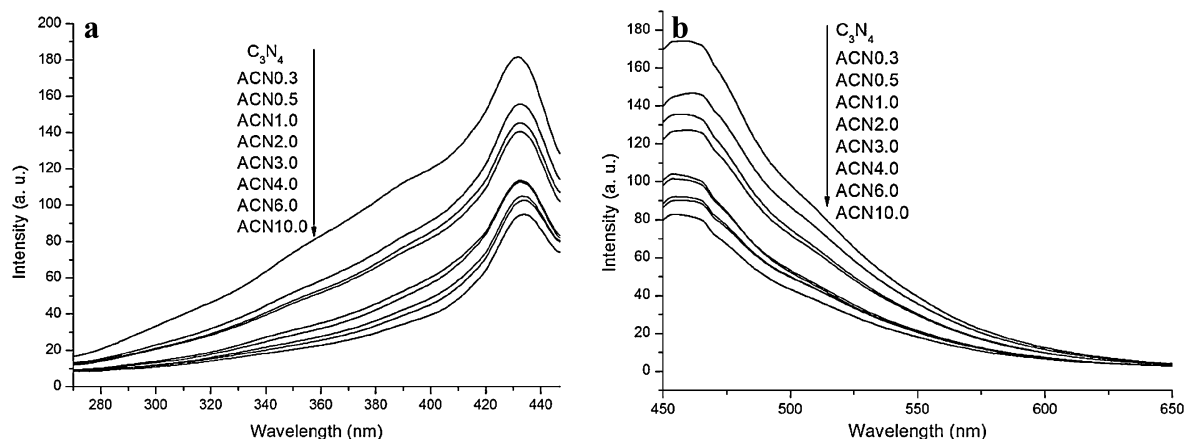

Fig. 5. Room-temperature PL excitation and emission spectra of the C_3N_4 and $Ag@C_3N_4$ photocatalysts ($\lambda_{ex} = 430\,nm$).
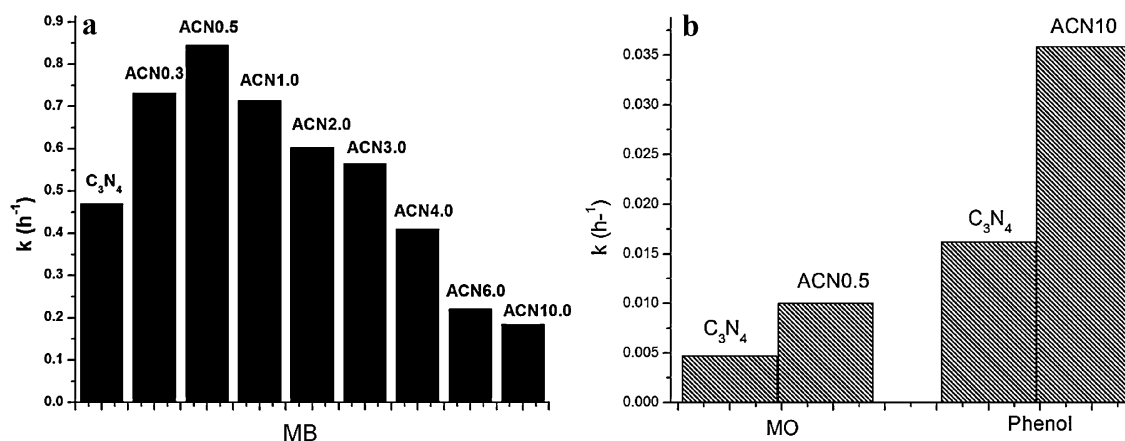
Fig. 6. Apparent rate constants for the photocatalytic degradation of MB (a), MO and phenol (b) over C_3N_4 and $Ag@C_3N_4$ photocatalysts under the visible light irradiation ($\lambda > 420$ nm, [MB] = 0.01 mM, [MO] = 0.03 mM, [phenol] = 10 ppm).
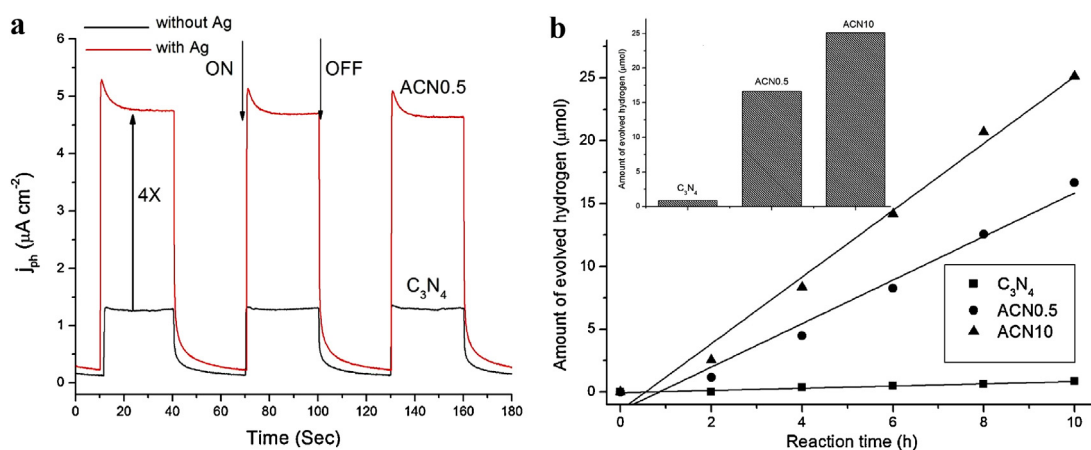

Fig. 7. (a) Photoresponses of C_3N_4 and $Ag@C_3N_4$-0.5 wt.% electrodes under the irradiation of visible light ($\lambda > 420$ nm) [$Na_2SO_4 = 0.1$ M]. (b) Photocatalytic activity of pure C_3N_4 and $Ag@C_3N_4$ photocatalysts for the hydrogen evolution reaction containing 20 vol.% triethanolamine as an electron donor under visible light illumination ($\lambda > 420$ nm).

improved, which is about 4 times as that of pure C_3N_4. As shown in Fig. 7b, photocatalytic results showed that only 0.84 μmol of hydrogen gas for 10 h could be generated for pure C_3N_4 without any modification in the presence of triethanolamine as a sacrificial reagent. However, $Ag@C_3N_4$ samples show a remarkable improvement in H_2 evolution activity over pure g-C_3N_4, the activity of $Ag@C_3N_4$-10 wt.% was improved by 30 times after introduction of Ag, which could promote charge transfer and creating hydrogen desorption sites. Because the photocurrent is formed mainly by the diffusion of photogenerated electrons to the back contact and simultaneously holes are taken up by the hole acceptor in the electrolyte [48,49]. The enhanced photocurrent and photocatalytic activity for hydrogen evolution over the $Ag@C_3N_4$ sample implies more efficient separation of the photoinduced electron–hole pairs and longer lifetime of the photogenerated charge carriers than that of pure C_3N_4, which is beneficial for its enhanced photocatalytic activity.

As shown in Fig. 8, it is observed that a significant negative correlation between zeta potential and photocatalytic activity. The sample Ag@C3N4-0.5 wt.% with optimum activity shows the least positive zeta potential. Therefore, colloidal stability of the $Ag@C_3N_4$ plays a key point in the photocatalysis reaction. MB molecule, as a cationic dye, it could hinder the precipitation of $Ag@C_3N_4$ spherical particles in water as a result of the inherited less positive surface charge that keeps the particles suspended in water. The stable suspension comes from electrostatic stabilization of the particles [50].

Therefore, MB dye cations would be easily adsorbed on the photocatalyst surface, resulting in enhancement of the reaction rate of photoexcited electrons with cations [51]. Compared with that of pure C_3N_4, $Ag@C_3N_4$ shows an enhanced adsorptivity (Fig. S6). After adsorption equilibrium, 76% and 66% of MB remained in the solution with pure C_3N_4 and $Ag@C_3N_4$ photocatalysts, respectively.
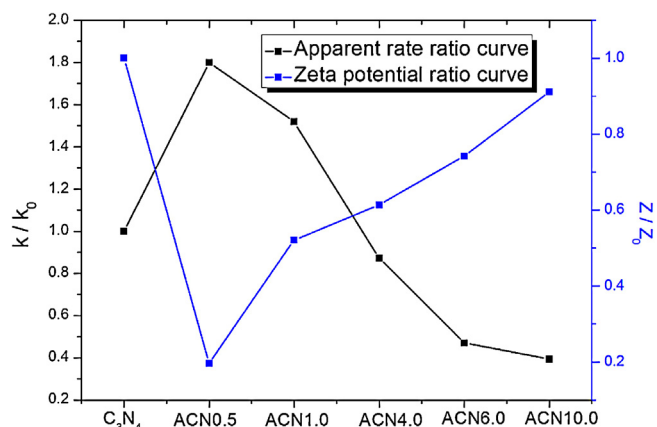

Fig. 8. Apparent rate and zeta potential in water suspension of C_3N_4 and $Ag@C_3N_4$ photocatalysts in the dark.
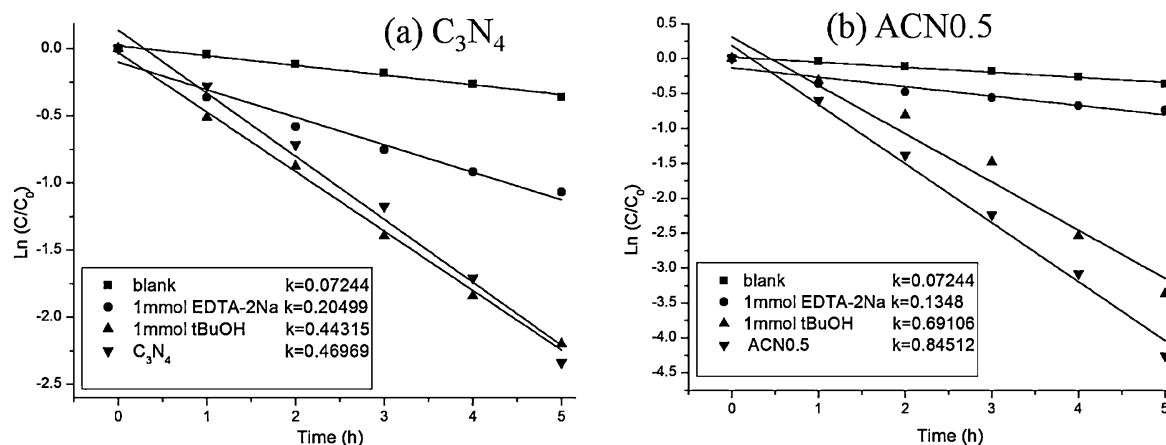
Fig. 9. Kinetic curves for the photocatalytic degradation of MB over C_3N_4 and $Ag@C_3N_4$-0.5 wt.% photocatalysts with the additon of hole and radical scavenger under the irradiation of visible light ($\lambda > 420$ nm).

Thus, the different zeta potential of $Ag@C_3N_4$ suspension could be responsible for the enhancement of adsorption in MB solution.

4.3. Proposed mechanism

To reveal the photocatalytic mechanism further, the main oxidative species in the photocatalytic process are detected through the trapping experiments of radicals using tBuOH as hydroxyl radical scavenger [52] and EDTA-2Na as holes radical scavenger [53]. As shown in Fig. 9a and b, the photocatalytic activity of C_3N_4 and $Ag@C_3N_4$ samples decreases slightly by the addition of hydroxyl radical scavenger, while reduced largely with the addition of hole capture, indicating that holes are the main oxidative species for both of C_3N_4 and $Ag@C_3N_4$ samples. In addition, compared with pure C_3N_4, the straight slope of $Ag@C_3N_4$ sample with same addition of EDTA-2Na declines obviously, indicating that there may exist more holes in $Ag@C_3N_4$ system.

To further understand the role of Ag nanoparticles in the $Ag@C_3N_4$ samples, electrochemical impedance spectroscopy (EIS) Nyquist plots of pure C_3N_4 and $Ag@C_3N_4$ samples has been carried out. As shown in Fig. 10, the Nyquist impedance plots of pure C_3N_4 and $Ag@C_3N_4$ samples electrode materials cycled in 0.1 M Na_2SO_4
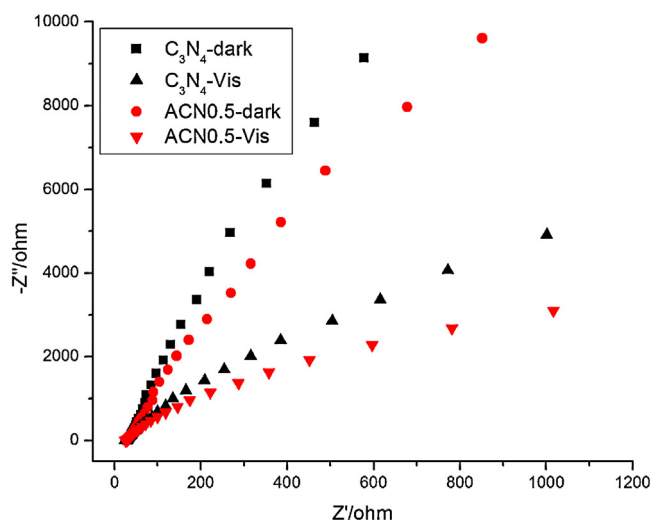

Fig. 10. EIS Nynquist plots of the C_3N_4 and $Ag@C_3N_4$-0.5 wt.% photocatalysts with light on/off cycles under the irradiation of visible light ($\lambda > 420$ nm) [$Na_2SO_4 = 0.1$ M].

electrolyte solution both exhibit semicycles at high frequencies. Considering that the preparation of the electrodes and electrolyte used are identical, the high frequency semicircle is relevant to the resistance of the electrodes [54]. In electrochemical spectra, the high frequency arc corresponds to the charge transfer limiting process and can be attributed to the double-layer capacitance (C_{dl}) in parallel with the charge transfer resistance (R_{ct}) at the contact interface between the electrode and electrolyte solution [55]. Clearly, the introduction of Ag nanoparticles leads to a significantly decreased diameter of the semicircular Nyquist plot as compared to pure C_3N_4, in the cases of both with and without light irradiation, suggesting a faster charge transfer rate.

From the point of structural features, $Ag@C_3N_4$ core–shell nanocomposites are endowed with remarkable advantages as heterogeneous photocatalysts. Firstly, encapsulating Ag nanoparticles within C_3N_4 shell can greatly enhance Ag stability against aggregation, and avoid undesirable corrosion or dissolution during the operation of reactions in practical photocatalytic applications. Secondly, as for the noble metal core Ag, its low lying Fermi energy level can serve as a reservoir of photoelectrons and prolong the lifetime of photogenerated carriers, thus possibly enhancing the C_3N_4 photocatalytic performance. Thirdly, the $Ag@C_3N_4$ core–shell nanoarchitecture provides "three-dimensional" intimate contact between the Ag core and C_3N_4 shell which maximizes the metal–support interaction, thereby facilitating the interfacial charge transfer process. Finally, the core–shell uniform structure composition provides a homogeneous environment for reactions to proceed. From the point of structural features, a probable mechanism for photocatalytic activity of pollutants over the $Ag@C_3N_4$ is proposed as illustrated in Scheme 1. Under the visible light irradiation, the electrons of C_3N_4 shell can be promoted to the conduction band, leaving holes in the valence band. In addition, $Ag@C_3N_4$ photocatalysts have loose core–shell structures, which means C_3N_4 nanosheets were not coated tightly on Ag nanoparticle and it possess porous structure between the layers. The photogenerated electrons can be trapped by the Ag metal cores located inside the C_3N_4, not only reduce the recombination of photoinduced electrons and holes but also prolong the lifetime of photogenerated pairs. Subsequently, photoinduced electrons on Ag nanoparticle surface can be exported through the porous structure of C_3N_4 interlayers and then be trapped by adsorbed O_2 in water to produce superoxide radical ($\bullet O_2^-$). Meanwhile, photoinduced holes can also readily react with surface-bound OH^- to generate hydroxyl radical species ($\bullet OH$) (Fig. S7). Thus, the superoxide radicals and hydroxyl radicals could be participated in photocatalytic

reaction in water by the way of reducing and oxidizing, respectively.

5. Conclusions

In summary, Ag@C_3N_4 nanocomposite has been prepared via a facile reflux treatment from C_3N_4 nanosheets. The formation of Ag@C_3N_4 nanocomposite is resulted from a synergistic interaction of coordination and coupling processes, and then monolayer-coated core coalescence and shell re-encapsulation. The exfoliation of precursors C_3N_4 and the intrinsic nature of Ag metal colloids play essential roles in the formation process. The photocurrent intensity, photocatalytic activity for the photodegradation of MB and hydrogen evolution reaction of Ag@C_3N_4 was about 4, 1.8 and 30 times as that of pure C_3N_4 sample, respectively. The enhancement of photocatalytic activity for Ag@C_3N_4 samples originates from a combined result of the LSPR effect for Ag and hybrid effect from C_3N_4. It is expected that our present work could provide useful information for the fabrication of other metal core@semiconductor shell nanocomposites.

Appendix A. Supplementary data

Supplementary data associated with this article can be found, in the online version, at http://dx.doi.org/10.1016/j.apcatb.2013.08.007.

References

[1] M.R. Hoffmann, S.T. Martin, W. Choi, D.W. Bahnemann, Environmental applications of semiconductor photocatalysis, Chem. Rev. 95 (1995) 69–96.
[2] P.V. Kamat, R. Huehn, R. Nicolaescu, A sense and shoot approach for photocatalytic degradation of organic contaminants in water, J. Phys. Chem. B 106 (2002) 788–794.
[3] F. Seker, K. Meeker, T.F. Kuech, A.B. Ellis, Surface chemistry of prototypical bulk II–VI and III–V semiconductors and implications for chemical sensing, Chem. Rev. 100 (2000) 2505–2536.
[4] P.V. Kamat, Photoinduced transformations in semiconductormetal nanocomposite assemblies, Pure Appl. Chem. 74 (2002) 1693–1706.
[5] P.V. Kamat, Photophysical, photochemical and photocatalytic aspects of metal nanoparticles, J. Phys. Chem. B 106 (2002) 7729–7744.
[6] M. Jakob, H. Levanon, P.V. Kamat, Charge distribution between UV-irradiated TiO_2 and gold nanoparticles: determination of shift in the Fermi level, Nano Lett. 3 (2003) 353–358.
[7] V. Subramanian, E.E. Wolf, P.V. Kamat, Catalysis with TiO_2/gold nanocomposites, J. Am. Chem. Soc. 126 (2004) 4943–4950.
[8] S. Link, M.A. El-Sayed, Spectral properties and relaxation dynamics of surface plasmon electronic oscillations in gold and silver nanodots and nanorods, J. Phys. Chem. B 103 (1999) 8410–8426.
[9] M. Haruta, Size and support-dependency in the catalysis of gold, Catal. Today 36 (1997) 153–166.
[10] T. Yonezawa, H. Matsune, T. Kunitake, Layered nanocomposite of close-packed gold nanoparticles and TiO_2 gel layers, Chem. Mater. 11 (1999) 33–35.
[11] A. Iwakoshi, T. Nanke, T. Kobayashi, Coating materials containing gold nanoparticles, Gold Bull. 38 (2005) 107–112.
[12] Y. Ohko, T. Tatsuma, A. Fujishima, Characterization of TiO_2 photocatalysis in the gas phase as a photoelectrochemical system: behavior of salt-modified systems, J. Phys. Chem. B 105 (2001) 10016–10021.
[13] P.D. Cozzoli, E. Fanizza, R. Comparelli, M.L. Curri, A. Agostiano, D. Laub, Role of metal nanoparticles in TiO_2/Ag nanocomposite-based microheterogeneous photocatalysis, J. Phys. Chem. B 108 (2004) 9623–9630.
[14] P.V. Kamat, M. Flumiani, A. Dawson, Metal–metal and metal–semiconductor composite nanoclusters, Colloid Surf. A 202 (2002) 269–279.
[15] V. Subramanian, E. Wolf, P.V. Kamat, Semiconductor–metal composite nanostructures. To what extent do metal nanoparticles improve the photocatalytic activity of TiO_2 films? J. Phys. Chem. B 105 (2001) 11439–11446.
[16] J.T. Li, S.K. Cushing, J. Bright, F. Meng, T.R. Senty, P. Zheng, A.D. Bristow, N.Q. Wu, Ag@Cu_2O core–shell nanoparticles as visible-light plasmonic photocatalysts, ACS Catal. 3 (2013) 47–51.
[17] N. Zhang, S.Q. Liu, Y.J. Xu, Recent progress on metal core@semiconductor shell nanocomposites as a promising type of photocatalyst, Nanoscale 4 (2012) 2227–2238.
[18] K. Dick, T. Dhanasekaran, Z. Zhang, D. Meisel, Size-dependent melting of silica-encapsulated gold nanoparticles, J. Am. Chem. Soc. 124 (2002) 2312–2317.
[19] T. Hirakawa, P.V. Kamat, Charge separation and catalytic activity of Ag@TiO_2 core–shell composite clusters under UV-irradiation, J. Am. Chem. Soc. 127 (2005) 3928–3934.
[20] H. Sakai, T. Kanda, H. Shibata, T. Ohkubo, M. Abe, Preparation of highly dispersed core/shell-type titania nanocapsules containing a single Ag nanoparticle, J. Am. Chem. Soc. 128 (2006) 4944–4945.
[21] R.F. Dong, B.Z. Tian, C.Y. Zeng, T.Y. Li, T.T. Wang, J.L. Zhang, Ecofriendly synthesis and photocatalytic activity of uniform cubic Ag@AgCl plasmonic photocatalyst, J. Phys. Chem. C 117 (2013) 213–220.
[22] L. Ge, C.C. Han, J. Liu, Y.F. Li, Enhanced visible light photocatalytic activity of novel polymeric g-C_3N_4 loaded with Ag nanoparticles, Appl. Catal. A: Gen. 409–410 (2011) 215–222.
[23] Y.L. Meng, J. Shen, D. Chen, G. Xin, Photodegradation performance of methylene blue aqueous solution on Ag/g-C_3N_4 catalyst, Rare Mater. 30 (2011) 276–279.
[24] A.Y. Liu, M.L. Cohen, Prediction of new low compressibility solids, Science 245 (1989) 841–842.
[25] J.S. Zhang, X.F. Chen, K. Takanabe, K. Maeda, K. Domen, J.D. Epping, X.Z. Fu, M. Antonietti, X.C. Wang, Synthesis of a carbon nitride structure for visible-light catalysis by copolymerization, Angew. Chem. Int. Ed. 49 (2010) 441–444.
[26] F.Z. Su, S.C. Mathew, L. Mohlmann, M. Antonietti, X.C. Wang, S. Blechert, Aerobic oxidative coupling of amines by carbon nitride photocatalysis with visible light, Angew. Chem. Int. Ed. 50 (2011) 657–660.
[27] X.F. Chen, J.S. Zhang, X.Z. Fu, M. Antonietti, X.C. Wang, Fe-g-C_3N_4-catalyzed oxidation of benzene to phenol using hydrogen peroxide and visible light, J. Am. Chem. Soc. 131 (2009) 11658–11659.
[28] X.C. Wang, K. Maeda, A. Thomas, K. Takanabe, G. Xin, J.M. Carlsson, K. Domen, M. Antonietti, A metal-free polymeric photocatalyst for hydrogen production from water under visible light, Nat. Mater. 8 (2009) 76–82.
[29] X.C. Wang, K. Maeda, X.F. Chen, K. Takanabe, K. Domen, Y.D. Hou, X.Z. Fu, M. Antonietti, Polymer semiconductors for artificial photosynthesis: hydrogen evolution by mesoporous graphitic carbon nitride with visible light, J. Am. Chem. Soc. 131 (2009) 1680–1681.
[30] F.Z. Su, S.C. Mathew, G. Lipner, X.Z. Fu, M. Antonietti, S. Blechert, X.C. Wang, mpg-C_3N_4-catalyzed selective oxidation of alcohols using O_2 and visible light, J. Am. Chem. Soc. 132 (2010) 16299–16301.
[31] G. Liu, P. Niu, C.H. Sun, S.C. Smith, Z.G. Chen, G. Lu, H.M. Cheng, Unique electronic structure induced high photoreactivity of sulfur-doped graphitic C_3N_4, J. Am. Chem. Soc. 132 (2010) 11642–11648.
[32] F. Goettmann, A. Fischer, M. Antonietti, A. Thomas, Chemical synthesis of mesoporous carbon nitrides using hard templates and their use as a metal-free catalyst for Friedel–Crafts reaction of benzene, Angew. Chem. Int. Ed. 45 (2006) 4467–4471.
[33] X.D. Zhang, X. Xie, H. Wang, J.J. Zhang, B.C. Pan, Y. Xie, Enhanced photoresponsive ultrathin graphitic-phase C_3N_4 nanosheets for bioimaging, J. Am. Chem. Soc. 135 (2013) 18–21.
[34] Y.H. Zheng, L.R. Zheng, Y.Y. Zhan, X.Y. Lin, Q. Zheng, K.M. Wei, Ag/ZnO heterostructure nanocrystals: synthesis, characterization, and photocatalysis, Inorg. Chem. 46 (2007) 6980–6986.
[35] X.F. Wu, H.Y. Song, J.M. Yoon, Y.T. Yu, Y.F. Chen, Synthesis of core–shell Au@TiO_2 nanoparticles with truncated wedge-shaped morphology and their photocatalytic properties, Langmuir 25 (2009) 6438–6447.
[36] D.J. Milliron, S.M. Hughes, Y. Cui, L. Manna, J. Li, L.W. Wang, P. Alivisatos, Colloidal nanocrystal heterostructures with linear and branched topology, Nature 430 (2004) 190–195.
[37] K.W. Kwon, M. Shim, γ-Fe_2O_3/II–VI sulfide nanocrystal heterojunctions, J. Am. Chem. Soc. 127 (2005) 10269–10275.
[38] P.D. Cozzoli, T. Pellegrino, L. Manna, Synthesis, properties and perspectives of hybrid nanocrystal structures, Chem. Soc. Rev. 35 (2006) 1195–1208.
[39] G.X. Wang, X.P. Shen, J. Yao, J. Park, Graphene nanosheets for enhanced lithium storage in lithium ion batteries, Carbon 47 (2009) 2049–2053.
[40] O. Akhavan, Graphene nanomesh by ZnO nanorod photocatalysts, ACS Nano 4 (2010) 4174–4180.
[41] X. Ling, L.M. Xie, Y. Fang, H. Xu, H.L. Zhang, J. Kong, M.S. Dresselhaus, J. Zhang, Z.F. Liu, Can graphene be used as a substrate for Raman enhancement? Nano Lett. 10 (2010) 553–561.
[42] J. Li, H.C. Zeng, Size tuning, functionalization, and reactivation of Au in TiO_2 nanoreactors, Angew. Chem. Int. Ed. 44 (2005) 4342–4345.
[43] P. Mulvaney, L.M. Liz-Marzan, M. Giersig, T. Ung, Silica encapsulation of quantum dots and metal clusters, J. Mater. Chem. 10 (2000) 1259–1270.
[44] L.M. Liz-Marzan, M. Giersig, P. Mulvaney, Synthesis of nanosized gold-silica core–shell particles, Langmuir 12 (1996) 4329–4335.
[45] L. Zhang, H. Wang, Cuprous oxide nanoshells with geometrically tunable optical properties, ACS Nano 5 (2011) 3257–3267.
[46] M.E. Aguirre, H.B. Rodríguez, E.S. Roman, A. Feldhoff, M.A. Grela, Ag@ZnO core–shell nanoparticles formed by the timely reduction of Ag ions and zinc acetate hydrolysis in N,N′-dimethylformamide: mechanism of growth and photocatalytic properties, J. Phys. Chem. C 115 (2011) 24967–24974.

[47] R. Georgekutty, M.K. Seery, S.C. Pillai, A highly efficient Ag–ZnO photocat-alyst: synthesis, properties, and mechanism, J. Phys. Chem. C 112 (2008) 13563–13570.

[48] S. Soedergren, A. Hagfeldt, J. Olsson, S.-E. Lindquist, Theoretical models for the action spectrum and the current–voltage characteristics of microporous semiconductor films in photoelectrochemical cells, J. Phys. Chem. 98 (1994) 5552–5556.

[49] N. Zhang, S.Q. Liu, X.Z. Fu, Y.J. Xu, Fabrication of coenocytic Pd@CdS nanocom-posite as a visible light photocatalyst for selective transformation under mild conditions, J. Mater. Chem. 22 (2012) 5042–5052.

[50] A.K. Sinha, M. Pradhan, S. Sarkar, T. Pal, Large-scale solid-state synthesis of Sn–SnO$_2$ nanoparticles from layered SnO by sunlight: a material for dye degra-dation in water by photocatalytic reaction, Environ. Sci. Technol. 47 (2013) 2339–2345.

[51] F. Amano, A. Yamakata, K. Nogami, M. Osawa, B. Ohtani, Effect of photoexcited electron dynamics on photocatalytic efficiency of Bismuth Tungstate, J. Phys. Chem. C 115 (2011) 16598–16605.

[52] H. Lee, W. Choi, Photocatalytic oxidation of arsenite in TiO$_2$ suspension: kinetics and mechanisms, Environ. Sci. Technol. 36 (2002) 3872–3878.

[53] J.H. Zhou, C.Y. Deng, S.H. Si, Y. Shi, X.L. Zhao, Study on the effect of EDTA on the photocatalytic reduction of mercury onto nanocrystalline titania using quartz crystal microbalance and differential pulse voltammetry, Electrochim. Acta 56 (2011) 2062–2067.

[54] D. Wang, D. Choi, J. Li, Z. Yang, Z. Nie, R. Kou, D. Hu, C. Wang, L.V. Saraf, J. Zhang, I.A. Aksay, J. Liu, Self-assembled TiO$_2$-graphene hybrid nanostructures for enhanced Li-ion insertion, ACS Nano 3 (2009) 907–914.

[55] H.L. Guo, X.F. Wang, Q.Y. Qian, F.B. Wang, X.H. Xia, A green approach to the synthesis of graphene nanosheets, ACS Nano 3 (2009) 2653–2659.